Force Detection of Electromagnetic Chirality of Tightly Focused Laser Beams

Abid Anjum Sifat,[†] Filippo Capolino,[†] and Eric O. Potma[*,†,‡]

†*Department of Electrical Engineering and Computer Science, University of California, Irvine, CA 92697, United States*

‡*Department of Chemistry, University of California, Irvine, CA 92697, United States*

E-mail: epotma@uci.edu

Abstract

We theoretically show that the optical chiral properties of tightly focused laser beams can be characterized by means of force detection. To measure the chiral properties of a beam of given handedness in the microscopic focal volume, we determine the photo-induced force exerted on a sharp tip, which is illuminated first by the beam of interest and second by an auxiliary beam of opposite handedness, in a sequential manner. We show that the difference between the force measurements is directly proportional to the chiral properties of the beam of interest. In particular, the gradient force difference $\Delta\langle F_{grad,z}\rangle$ is found to have exclusive correspondence to the time-averaged helicity density of the incident light, whereas the differential scattering force provides information about the spin angular momentum density of light. We further characterize and quantify the helicity-dependent $\Delta\langle F_{grad,z}\rangle$ using a Mie scattering formalism complemented with full wave simulations, underlining that the magnitude of the difference force is within an experimentally detectable range.

Keywords

optical chirality, helicity density, photo-induced force

Introduction

Light can exist in a chiral state, and this property makes it possible to study chiral objects, such as molecules and nanostructures, in an optical manner.[1–6] Optical detection of chirality is important in a variety of scientific fields, with key applications in molecular biology and pharmacology.[7–10] In common applications, the specimen is illuminated sequentially with left-handed and right-handed circularly polarized light (LCP and RCP), and the chiral information is inferred from the differential response of the material. The chiral state of circularly polarized light is well understood, which facilitates the analysis of such measurements. However, performing similar measurements at dimensions beyond the diffraction limit can be challenging,[11–13] because the chiral state of light in the near zone cannot always be assessed with far-field measurements.

The chiral state of light is related to the curled character of the electric and magnetic fields. The quantity commonly used for quantifying this 'degree of curliness' is the time-averaged helicity density,[13–15] which is defined as $h = \frac{1}{2\omega c}\mathrm{Im}(\mathbf{E}\cdot\mathbf{H}^*)$, where $\mathbf{E}$ and $\mathbf{H}$ are the phasor electric and magnetic field at angular frequency ω, and c is the speed of light (* denotes complex conjugation).[16,17] The helicity density is a time-even, pseudo-scalar conserved quantity; when using CP light, it corresponds to the difference between the numbers of RCP and LCP photons.[14,15,18] The flux of the helicity density, i.e. the chiral momentum density, is related to the spin angular momentum of the beam.[14,18] The latter quantity is a time-odd, pseudo-vector quantity[15] and its density is defined as $\boldsymbol{\sigma} = -\frac{\varepsilon_0}{4\omega i}(\mathbf{E}\times\mathbf{E}^*) - \frac{\mu_0}{4\omega i}(\mathbf{H}\times\mathbf{H}^*)$, where ε_0 and μ_0 are the absolute permittivity and permeability of free space,[15,19] respectively. Although both quantities describe angular momentum associated with the polarization state of light,[14] only the time-averaged helicity density is classified as a conserved property of the

electromagnetic field,[1,20] and, therefore, considered to be the proper descriptor of optical chirality.

In this work, we are interested in characterizing the helicity density in the focal volume of a tightly focused laser beam. The question arises whether a quantity like the helicity density can be properly measured at dimensions beyond the diffraction limit of light. Although near-field and scanning nanoparticle methods have been used to probe the electric and magnetic components of vector fields at sub-diffraction limited resolution,[21–25] a direct measurement of the helicity density in the near-field of tightly focused laser fields has so far remained out of reach. Unlike quantities such as energy, mechanical force and torque carried or performed by the electromagnetic field, properties like linear and angular momentum of light are more difficult to measure and are commonly deduced from other measurable quantities.[26] Helicity density of light falls into the latter category, and measuring it requires a connection to a quantity that can be experimentally assessed.

It has been shown that, by scanning a Si nanoparticle through focus and analyzing its scattered light in the far-field, it is possible to extract information about the transverse spin density of the focused field,[27] yet no general approach for mapping the helicity density in focus has been reported thus far. One possibility is to detect helicity density through photo-induced force, which is what we propose here. For instance, the technique of photo-induced force microscopy (PiFM) has been used to map electric and magnetic field distributions of focused Gaussian as well as vector beams through the optical force exerted on a metallic tip[28,29] or a specially designed magnetic nanoprobe.[25] The photo-induced force has also been used for sorting and trapping of chiral nanoparticles.[30–34] In addition, PiFM has been employed to determine enantioselective chirality of nanosamples,[35] for measuring the geometric chirality of broken symmetry structures with differential force measurements under RCP/LCP illumination[36] and for measuring enantioselective optical forces .[37]

We theoretically investigate the connection between the photo-induced forces felt by a chiral tip under differential RCP/LCP illumination and the chiral state of light at the

nanoscale. Using image dipole theory, we have found a direct relation between the measured differential force and the chiral properties of the incident electromagnetic field in terms of the time-averaged helicity density and spin-angular momentum density. The $\exp(-i\omega t)$ time notation is implicitly assumed throughout the paper. We further model the chiral tip as an isotropic chiral sphere to examine several design considerations and validate our dipole model with full-wave, finite element method (FEM) simulations.

Theoretical Analysis

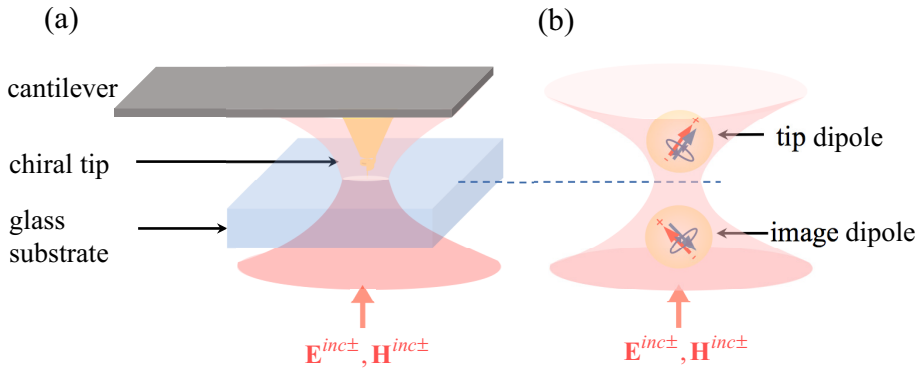

Figure 1: (a) Schematic of the PiFM system with a chiral tip with illumination from the bottom. (b) Photo-induced chiral tip dipole and image dipole according to image dipole theory.

We are interested in detecting the mechanical force that acts on the chiral tip due to the presence of the electromagnetic field, as shown schematically in Figure 1(a). We can model the tip as particle and write the time-averaged force exerted on this particle as[38,39]

$$\langle \mathbf{F} \rangle = \frac{1}{2}\mathrm{Re}\Big\{ \int_S \Big[\varepsilon(\mathbf{E}\cdot\hat{\mathbf{n}})\mathbf{E}^* + \mu^{-1}(\mathbf{B}\cdot\hat{\mathbf{n}})\mathbf{B}^* - \frac{1}{2}\left(\varepsilon|\mathbf{E}|^2 + \mu^{-1}|\mathbf{B}|^2\right)\hat{\mathbf{n}} \Big] \, dS \Big\} \tag{1}$$

where the integration is over the arbitrary surface S that encloses the tip-particle of volume V, $\hat{\mathbf{n}}$ is the unit vector normal to this surface, and $\mathbf{E}$ and $\mathbf{B}$ are the phasors of the total electric field and magnetic flux density, which include both the incident light and the scattered light contributions. It is assumed that the particle is embedded in a non-dissipative medium with

permittivity ε and permeability μ. To simplify this expression, we next assume that the tip can be described as a dipolar particle with an electric and magnetic dipole moment in free space, written as $\mathbf{p}_{tip}$ (Cm) and $\mathbf{m}_{tip}$ (Am^2), respectively. The phasors of the dipole moments are defined as $\mathbf{p}_{tip} = \int \mathbf{r}\rho(\mathbf{r})dV$ and $\mathbf{m}_{tip} = \frac{1}{2}\int[\mathbf{r} \times \mathbf{J}(\mathbf{r})]dV$, where $\rho(\mathbf{r})$ and $\mathbf{J}(\mathbf{r})$ are the induced charge and current densities in the particle. Assuming the tip-particle's response is dominated by its electric and magnetic dipole moments, the expression for the time-averaged electromagnetic force reduces to[40,41]

$$\langle \mathbf{F} \rangle = \frac{1}{2}\mathrm{Re}\Big\{ \big(\nabla \mathbf{E}^{loc}(\mathbf{r}_{tip})\big)^* \cdot \mathbf{p}_{tip} + \big(\nabla \mathbf{H}^{loc}(\mathbf{r}_{tip})\big)^* \cdot \mu_0 \mathbf{m}_{tip} - \frac{c\mu_0 k^4}{6\pi}(\mathbf{p}_{tip} \times \mathbf{m}_{tip}^*)\Big\} \tag{2}$$

where $\mathbf{E}^{loc}(\mathbf{r}_{tip})$ and $\mathbf{H}^{loc}(\mathbf{r}_{tip})$ are the local electric and magnetic field at the tip dipole position. Here, $\nabla\mathbf{E}$ and $\nabla\mathbf{H}$ are the gradient of electric and magnetic field vectors. This is of dyadic form and defined as $\nabla\mathbf{E} = \sum_i \sum_j \frac{\partial E_j}{\partial x_i}\hat{x_i}\hat{x_j}$ where i and j stands for x, y and z components of cartesian coordinates.[42] Note that sometimes in the literature the μ_0 factor in the second and third term of equation (2) is included in the definition of the magnetic dipole moment ($\mathbf{m}_{tip}$).[35,43,44] The notation used in this paper is the same as that in Refs.[12,13,17,25,45] The time-averaged force has three distinct contributions: the first term on the right hand side of equation (2) is recognized as the electric dipolar force $\langle \mathbf{F}_e \rangle$, the second term is known as the magnetic dipolar force $\langle \mathbf{F}_m \rangle$, and the last term is called the interaction force $\langle \mathbf{F}_{int} \rangle$.

To calculate the force, we require expressions for the induced electric and magnetic dipole moments. Assuming that the tip is an isotropic and reciprocal chiral object, the dipole moments can be related to the local fields through polarizabilities as[46]

$$\mathbf{p}_{tip} = \alpha_{ee}\mathbf{E}^{loc}(\mathbf{r}_{tip}) + \alpha_{em}\mathbf{H}^{loc}(\mathbf{r}_{tip}) \tag{3}$$

$$\mathbf{m}_{tip} = -\mu_0^{-1}\alpha_{em}\mathbf{E}^{loc}(\mathbf{r}_{tip}) + \alpha_{mm}\mathbf{H}^{loc}(\mathbf{r}_{tip}) \tag{4}$$

where α_{ee}, α_{mm} and α_{em} are the electric, magnetic and electro-magnetic polarizabilities, respectively. We have considered that $\alpha_{me} = -\mu_0^{-1}\alpha_{em}$ because of reciprocity. The local fields at the tip dipole position can be obtained from image dipole theory.[38,47,48] We model the effect of the substrate by substituting the substrate response by the image of the photo-induced (chiral) dipole in the tip, written as $\mathbf{p}_{img}$ and $\mathbf{m}_{img}$ and shown in Figure 1(b). The local electric and magnetic fields at the tip position can then be expressed as

$$\mathbf{E}^{loc}(\mathbf{r}_{tip}) = \mathbf{E}^{inc}(\mathbf{r}_{tip}) + \mathbf{E}^{sca}_{img\to tip}(\mathbf{r}_{tip}) \tag{5}$$

$$\mathbf{H}^{loc}(\mathbf{r}_{tip}) = \mathbf{H}^{inc}(\mathbf{r}_{tip}) + \mathbf{H}^{sca}_{img\to tip}(\mathbf{r}_{tip}) \tag{6}$$

where $\mathbf{E}^{inc}(\mathbf{r}_{tip})$, $\mathbf{H}^{inc}(\mathbf{r}_{tip})$ are the incident electric and magnetic field at the tip dipole location, and $\mathbf{E}^{sca}_{img\to tip}(\mathbf{r}_{tip})$, $\mathbf{H}^{sca}_{img\to tip}(\mathbf{r}_{tip})$ are the scattered electric and magnetic field by the image dipoles at the tip dipole location.

The scattered fields, which include nearfields, are defined through the image dipole moments and their Green's functions as[38,47]

$$\mathbf{E}^{sca}_{img\to tip}(\mathbf{r}_{tip}) = \underline{\mathbf{G}}^{ee}(\mathbf{r}_{tip} - \mathbf{r}_{img}) \cdot \mathbf{p}_{img} + \underline{\mathbf{G}}^{em}(\mathbf{r}_{tip} - \mathbf{r}_{img}) \cdot \mathbf{m}_{img} \tag{7}$$

$$\mathbf{H}^{sca}_{img\to tip}(\mathbf{r}_{tip}) = \underline{\mathbf{G}}^{me}(\mathbf{r}_{tip} - \mathbf{r}_{img}) \cdot \mathbf{p}_{img} + \underline{\mathbf{G}}^{mm}(\mathbf{r}_{tip} - \mathbf{r}_{img}) \cdot \mathbf{m}_{img} \tag{8}$$

where $\underline{\mathbf{G}}(\mathbf{r}) = G_x\hat{\mathbf{x}}\hat{\mathbf{x}} + G_y\hat{\mathbf{y}}\hat{\mathbf{y}} + G_z\hat{\mathbf{z}}\hat{\mathbf{z}}$ is the dyadic Green's function in Cartesian coordinates. The Green's functions that appear in equations (7) and (8) are approximated in the nearfield

as[49]

$$\underline{\mathbf{G}}^{ee}(\mathbf{r}) = \frac{1}{4\pi\varepsilon_0|\mathbf{r}|^3}(3\hat{\mathbf{r}}\hat{\mathbf{r}} - \underline{\mathbf{I}}) \tag{9}$$

$$\underline{\mathbf{G}}^{mm}(\mathbf{r}) = \frac{1}{4\pi|\mathbf{r}|^3}(3\hat{\mathbf{r}}\hat{\mathbf{r}} - \underline{\mathbf{I}}) \tag{10}$$

$$\underline{\mathbf{G}}^{em}(\mathbf{r}) = -\frac{1}{i\omega\varepsilon_0}\nabla \times \underline{\mathbf{G}}^{mm}(\mathbf{r}) \tag{11}$$

$$\underline{\mathbf{G}}^{me}(\mathbf{r}) = \frac{1}{i\omega\mu_0}\nabla \times \underline{\mathbf{G}}^{ee}(\mathbf{r}) \tag{12}$$

where $\underline{\mathbf{I}}$ is unit dyad (tensor) and $\hat{\mathbf{r}}$ is the unit vector from the source point to the point of observation.

In the same fashion, we can also define the image dipole moments and the local fields at the image location. Our goal is to obtain self-consistent approximate expressions for the local fields at the tip location and for the dipole moments in terms of the incident light components. To achieve this, consistent with the nearfield approximation of the Green's function, we first ignore any phase retardation effects in the fields between the tip and image dipole position. Second, we will only consider terms in the polarizability up to second order (full derivation is provided in the Supplementary Information). With these assumptions, we may use equations (3)-(6) to determine the longitudinal (z) component of the time-averaged

force in the dipole approximation as written as

$$
\begin{aligned}
\langle F_{z,grad}\rangle &= \langle F_{z,e}\rangle + \langle F_{z,m}\rangle \\
&= \frac{3}{2\pi|z|^4}\left[\frac{1}{2}\Big(-\frac{|\alpha_{ee}|^2}{\varepsilon_0}+\mu_0|\mu_0^{-1}\alpha_{em}|^2\Big)(\tfrac{1}{2}|\mathbf{E}_\parallel^{inc}|^2+|\mathbf{E}_z^{inc}|^2)\right. \\
&\qquad +\frac{1}{2}\Big(-\frac{|\alpha_{em}|^2}{\varepsilon_0}+\mu_0|\alpha_{mm}|^2\Big)(\tfrac{1}{2}|\mathbf{H}_\parallel^{inc}|^2+|\mathbf{H}_z^{inc}|^2) \\
&\qquad \left.-\mathrm{Re}\Big\{\Big(\frac{\alpha_{ee}\alpha_{em}^*}{\varepsilon_0}+\alpha_{mm}^*\alpha_{em}\Big)(\tfrac{1}{2}\mathbf{E}_\parallel^{inc}\cdot\mathbf{H}_\parallel^{inc*}+\mathbf{E}_z^{inc}\cdot\mathbf{H}_z^{inc*})\Big\}\right] \\
&+\frac{6\omega}{\pi k^2|z|^5}\left[2\omega\mathrm{Re}\Big\{\frac{\alpha_{ee}\alpha_{em}^*}{\varepsilon_0}\Big\}[\boldsymbol{\sigma}_E^{inc}]_z-2\omega\mathrm{Re}\big\{\alpha_{em}\alpha_{mm}^*\big\}[\boldsymbol{\sigma}_H^{inc}]_z\right. \\
&\qquad \left.-2\mathrm{Im}\Big\{(|\alpha_{em}|^2-\mu_0\alpha_{ee}\alpha_{mm}^*)[\mathbf{S}^{inc}]_z\Big\}\right]
\end{aligned}
\tag{13}
$$

$$
\begin{aligned}
\langle F_{z,int}\rangle = \; &-\frac{ck^4}{12\pi}\left[\mathrm{Re}\Big\{-\alpha_{em}^*\alpha_{ee}\Big\}\mathrm{Re}\Big\{[\mathbf{E}_\parallel^{inc}\times\mathbf{E}_\parallel^{inc*}]_z\Big\}\right. \\
&+\mathrm{Re}\Big\{\mu_0\alpha_{mm}^*\alpha_{em}\Big\}\mathrm{Re}\Big\{[\mathbf{H}_\parallel^{inc}\times\mathbf{H}_\parallel^{inc*}]_z\Big\} \\
&+4\omega\mathrm{Im}\Big\{-\frac{\alpha_{em}^*\alpha_{ee}}{\varepsilon_0}\Big\}[\boldsymbol{\sigma}_E^{inc}]_z+4\omega\mathrm{Im}\Big\{-\alpha_{mm}^*\alpha_{em}\Big\}[\boldsymbol{\sigma}_H^{inc}]_z \\
&\left.+2\mathrm{Re}\Big\{\alpha_{em}^*\alpha_{em}[\mathbf{S}^{inc*}]_z\Big\}+2\mathrm{Re}\Big\{\mu_0\alpha_{mm}^*\alpha_{ee}[\mathbf{S}^{inc}]_z\Big\}\right]
\end{aligned}
\tag{14}
$$

where $\mathbf{E}_\parallel^{inc}=E_x^{inc}\hat{\mathbf{x}}+E_y^{inc}\hat{\mathbf{y}}$, $\mathbf{H}_\parallel^{inc}=H_x^{inc}\hat{\mathbf{x}}+H_y^{inc}\hat{\mathbf{y}}$ and $\mathbf{E}_z^{inc}=E_z^{inc}\hat{\mathbf{z}}$, $\mathbf{H}_z^{inc}=H_z^{inc}\hat{\mathbf{z}}$ are the transverse and longitudinal components of the incident fields at the tip dipole location, the notation ($\mathbf{r}_{tip}$) has been avoided here for brevity; $\mathbf{S}^{inc}=\frac{1}{2}\mathbf{E}^{inc}\times(\mathbf{H}^{inc})^*$ is the Poynting vector of the incident field; $\boldsymbol{\sigma}_E^{inc}$ and $\boldsymbol{\sigma}_H^{inc}$ are the electric and magnetic parts of the time-averaged total spin angular momentum density of the incident light; and z is the vertical distance between the tip dipole and its image. See the Supporting Information for a detailed derivation of equations (13) and (14).

Equation (13) describes the force due to the combined electric and magnetic dipolar response of the tip. This force shows a distance dependence on the tip-sample distance which scales as z^{-4}, similar to the distance dependence of the gradient force that is typically measured in PiFM.[38,50] The first two lines of equation (13) are recognized as the purely electric and purely magnetic dipolar force contributions to the gradient force, whereas the third line describes the force that arises from a nonzero scalar product of the electric and magnetic fields, i.e. the helicity density. In addition, this force also exhibits a z^{-5} distance dependence, expressed in the last two lines of equation (13). This part carries information about the longitudinal component of the spin angular momentum density and the Poynting vector of the incident light.

Equation (14) accounts for the interaction force, which lacks a direct dependence on the tip-sample distance. In addition to the purely electric and magnetic contributions to the interaction force, described by the first two lines in equation (14), the latter two lines add force contributions that scale with the longitudinal component of the spin angular momentum density and with the Poynting vector. Because these latter terms depend on the momentum of the incoming field, the interaction force shows similarity with the scattering force[38,50] in PiFM.

We are interested in using the force as a way to measure the helicity density h^{inc} of an incident beam. To measure this quantity, we will use a second incident beam that is similar to the original beam but is of opposite handedness. Hence, if we define the helicity density of the original beam as $h^{inc} = h^{inc+}$, then the helicity density of the auxiliary beam is given as h^{inc-}. For this purpose, we assume two states for the incident light, indicated by $\mathbf{E}^{inc+}$, $\mathbf{H}^{inc+}$ and $\mathbf{E}^{inc-}$, $\mathbf{H}^{inc-}$, describing the input fields of different handedness. The two illumination states have the same energy densities, $|\mathbf{E}^{inc+}|^2 = |\mathbf{E}^{inc-}|^2$ and $|\mathbf{H}^{inc+}|^2 = |\mathbf{H}^{inc-}|^2$, but exhibit opposite helicity densities, $\mathrm{Im}(\mathbf{E}^{inc+} \cdot \mathbf{H}^{inc+*}) = -\mathrm{Im}(\mathbf{E}^{inc-} \cdot \mathbf{H}^{inc-*})$, i.e. $h^{inc+} = -h^{inc-}$. Note that the longitudinal spin angular momentum density components are related as $[\boldsymbol{\sigma}_E^{inc+}]_z = -[\boldsymbol{\sigma}_E^{inc-}]_z$ and $[\boldsymbol{\sigma}_H^{inc+}]_z = -[\boldsymbol{\sigma}_H^{inc-}]_z$. We also find that $\mathbf{S}^{inc+} = \mathbf{S}^{inc-}$,

and that the following relations hold

$$\begin{aligned}\mathrm{Re}\Big\{[\mathbf{E}_{\parallel}^{inc+}\times\mathbf{E}_{\parallel}^{inc+*}]_z\Big\}&=\mathrm{Re}\Big\{[\mathbf{E}_{\parallel}^{inc-}\times\mathbf{E}_{\parallel}^{inc-*}]_z\Big\}\\ \mathrm{Re}\Big\{[\mathbf{H}_{\parallel}^{inc+}\times\mathbf{H}_{\parallel}^{inc+*}]_z\Big\}&=\mathrm{Re}\Big\{[\mathbf{H}_{\parallel}^{inc-}\times\mathbf{H}_{\parallel}^{inc-*}]_z\Big\}\end{aligned} \tag{15}$$

We next determine the differential force, obtained by measuring the force under illumination with incident light of (+) and (−) handedness, and taking the difference. Under these conditions, the differential gradient force $\Delta\langle F_{z,grad}\rangle = \langle F_{z,grad}\rangle^{+} - \langle F_{z,grad}\rangle^{-}$ and the differential interaction force $\Delta\langle F_{z,int}\rangle = \langle F_{z,int}\rangle^{+} - \langle F_{z,int}\rangle^{-}$ can be obtained from equations (13) and (14) as

$$\begin{aligned}\Delta\langle F_{z,grad}\rangle = \;& \frac{6\omega c}{\pi|z|^4}\mathrm{Im}\Big\{\frac{\alpha_{em}^{*}}{\varepsilon_0}(\alpha_{ee}-\alpha_{mm}\varepsilon_0)\Big\}\Big(\tfrac{1}{2}h_{\parallel}^{inc}+h_z^{inc}\Big)\\ &+\frac{24\omega^2}{\pi k^2|z|^5}\left[\mathrm{Re}\left\{\frac{\alpha_{ee}\alpha_{em}^{*}}{\varepsilon_o}\right\}[\boldsymbol{\sigma}_E^{inc}]_z-\mathrm{Re}\left\{\alpha_{mm}\alpha_{em}^{*}\right\}[\boldsymbol{\sigma}_H^{inc}]_z\right]\end{aligned} \tag{16}$$

$$\Delta\langle F_{z,int}\rangle = \frac{2\omega c k^4}{3\pi}\Big[\mathrm{Im}\Big\{\frac{\alpha_{em}^{*}\alpha_{ee}}{\varepsilon_o}\Big\}[\boldsymbol{\sigma}_E^{inc}]_z+\mathrm{Im}\Big\{\alpha_{mm}\alpha_{em}^{*}\Big\}[\boldsymbol{\sigma}_H^{inc}]_z\Big] \tag{17}$$

where $h_{\parallel}^{inc} = \frac{1}{2\omega c}\mathrm{Im}\left\{\mathbf{E}_{\parallel}^{inc}\cdot\mathbf{H}_{\parallel}^{inc*}\right\}$ and $h_z^{inc} = \frac{1}{2\omega c}\mathrm{Im}\left\{\mathbf{E}_z^{inc}\cdot\mathbf{H}_z^{inc*}\right\}$ are the tangential and longitudinal helicity density, respectively. We find that the differential force is proportional to the difference in helicity density between the incident light and the auxiliary beam, i.e. $h^{inc+} - h^{inc-} = 2h^{inc}$. Since we had defined $h^{inc} = h^{inc+}$, we observe that the differential gradient force measured in this procedure is directly proportional to the desired h^{inc} of the incident chiral light. From equation (16) we see that the differential gradient force depends on the helicity density of the incident light, whereas (17) predicts that the differential interaction force carries only information on the spin angular momentum of the incident light. When using optimally chiral light[17] satisfying the relation $\mathbf{E} = \pm i\eta_0\mathbf{H}$ with $\eta_0 = \sqrt{\mu_0/\varepsilon_0}$, the two spin angular momentum densities are such that $\boldsymbol{\sigma}_H^{inc} = \boldsymbol{\sigma}_E^{inc}$. Note that circularly polarized light is a particular case of optimally chiral light.

When analyzing the first and the second terms in equation (16), we note that the pre-factor containing z^{-5} grows larger than the corresponding z^{-4} pre-factor for sub-wavelength distances. The magnitude of the two contributions to the differential gradient force are, however, also determined by the material polarizabilities. In this context, we must observe that for nanoparticles made of low loss materials like silicon, the values for the polarizabilities α_{ee} and α_{mm} are mainly real when the particle is much smaller than the optical wavelength (i.e., at the quasistatic limit). Assuming the same particle has chirality, we also observe that α_{em} is mainly imaginary (see for example the expression (9) in Ref.[35] or (7) in Ref.[44]). Therefore, when the chiral tip is made of a low-loss material and much smaller than the optical wavelength, the term $\mathrm{Im}\{\alpha_{ee}\alpha_{em}^*\}$ is larger than the term $\mathrm{Re}\{\alpha_{ee}\alpha_{em}^*\}$. Similarly, we find that $\mathrm{Im}\{\alpha_{mm}\alpha_{em}^*\} \gg \mathrm{Re}\{\alpha_{mm}\alpha_{em}^*\}$. Taken together, even though the considered tip size is not deeply sub-wavelength, we find that for practical sizes and material properties of the tip, as shown in Section (see also Supporting Information section 6), the first term in equation (16) is dominant over the second term. For this reason, we may approximate the differential gradient force as

$$\Delta\langle F_{z,grad}\rangle \sim \frac{6\omega c}{\pi|z|^4}\mathrm{Im}\Big\{\frac{\alpha_{em}^*}{\varepsilon_0}(\alpha_{ee}-\alpha_{mm}\varepsilon_0)\Big\}\Big(\tfrac{1}{2}h_{\parallel}^{inc}+h_z^{inc}\Big) \tag{18}$$

and the validity of such approximation will be confirmed by the numerical results. It is clear that the strength and sign of the differential gradient force depends on α_{em}^* and thus relies on the chiral properties of the tip. For small tip-sample distances, the differential gradient force is expected to constitute the dominant contribution to the measured force, thus offering a means of experimentally extracting information about the helicity density. Unless otherwise stated, we will use equation (18) to determine the differential force.

Mie Scattering Formalism

We next study the characteristics of the differential gradient force. We see from equation (18) that $\Delta\langle F_{z,grad}\rangle$ depends on the polarizability of the tip material, including the electromagnetic polarizability. To model the tip polarizability, we assume that the tip can be described as a spherical chiral nanoparticle (NP). We also assume that the following constitutive relations hold: $\mathbf{D} = \varepsilon_0\varepsilon_r\mathbf{E} + i\sqrt{\varepsilon_0\mu_0}\kappa\mathbf{H}$ and $\mathbf{B} = \mu_0\mu_r\mathbf{H} - i\sqrt{\varepsilon_0\mu_0}\kappa\mathbf{E}$, where ε_r and μ_r are the relative permittivity and relative permeability, respectively.[17,46] The chirality parameter κ is an empirical quantity that provides the chiral strength of the material under consideration. We can next relate the electric, magnetic and electro-magnetic polarizabilities through the material parameters by using Mie scattering theory as:[17,35,51] $\alpha_{ee} = -6\pi i\varepsilon_0 b_1/k_0^3$, $\alpha_{mm} = -6\pi i a_1/k_0^3$ and $\alpha_{em} = 6\pi i c_1/(ck_0^3)$ where c is the free space speed of light, k_0 is the wavenumber in free space and b_1, a_1, c_1 are the Mie coefficients. In our calculations, the material parameters of the isotropic chiral NP such as ε_r and μ_r are those of crystalline silicon[52] with $\mu_r = 1$.

We next place the sphere (i.e., the tip) just above a flat and transparent dielectric substrate such that the distance between the sphere's surface and the substrate surface is 5 nm. The system is subsequently illuminated from the bottom with a plane wave of field strength 1.5×10^6 Vm^{-1} (incident intensity of 3.0 mW/μm^2) that is either in the LCP ($\mathbf{E}^{inc+} = E^{inc}\hat{\mathbf{x}} + iE^{inc}\hat{\mathbf{y}}$) or RCP ($\mathbf{E}^{inc-} = E^{inc}\hat{\mathbf{x}} - iE^{inc}\hat{\mathbf{y}}$) state, and which propagates through the transparent dielectric material toward the sphere. The CP wave induces an electric and magnetic dipole in the chiral sphere, and the presence of the substrate can subsequently be modeled by including an image of the induced electric and magnetic dipoles,[25,28] analogous to the procedure used for the point dipole model in section . For simplicity, it is assumed that the image dipole strength is identical to the induced dipole in the sphere. In the current configuration, the distance between the location of the dipole and its image is $2(r_{NP} + 5$ nm), where r_{NP} is the radius of the sphere. We calculate the differential gradient force spectrum with the aid of equation (18) and plot it as a function of sphere radius and

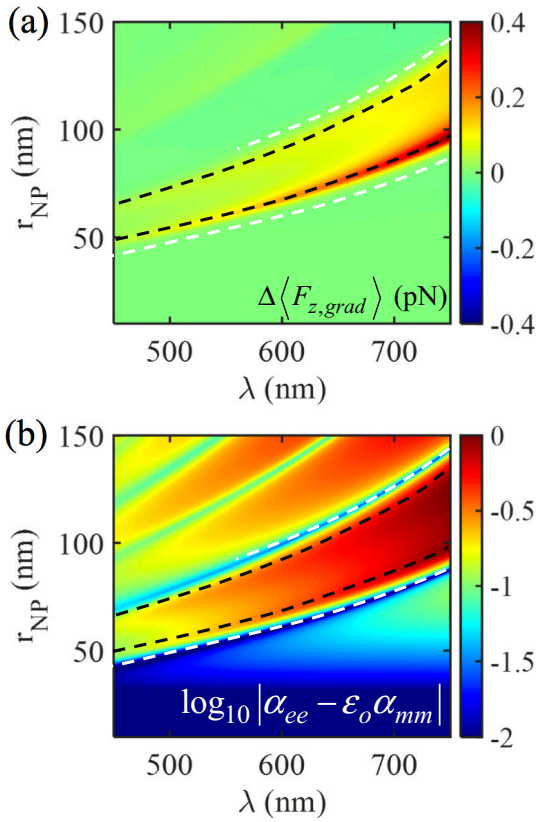

Figure 2: (a) Differential gradient force spectrum in pN. (b) Normalized magnitude spectrum of $\alpha_{ee} - \varepsilon_0 \alpha_{mm}$ for different radii of the chiral NP. The material properties of the chiral NP, ε_r and μ_r are considered the same as silicon with $\mu_r = 1$ and $\kappa = 0.1$. In all calculations, the tip-image dipole center-center distance is $|z| = 2r_{NP} + 10$ nm. Black dashed lines indicate resonance condition of c_1 and white dashed lines indicate the local minima in the plot, which approach the Kerker condition.

excitation wavelength in Fig. 2(a). In all calculations, the value of the bulk chirality κ of the sphere is considered real and set to 0.1.[53,54] It is clear that nonzero $\Delta\langle F_{z,grad}\rangle$ is achieved under certain experimental conditions. In particular, the maxima are seen to co-localize with the resonant spectral position of the electro-magnetic Mie coefficient c_1 of the chiral NP. The black dotted lines show the location of the peak values of $\mathrm{Im}(c_1)$. Changing κ does not alter the spectral resonances, but instead changes the sign and magnitude of the differential force proportionally.

A careful inspection of equation (18) suggests that, for any chosen r_{NP} and κ of the tip, $\Delta\langle F_{z,grad}\rangle$ may approach zero when the first Kerker condition of the chiral NP is met, irrespective of helicity density of the incident light. The Kerker condition is $\alpha_{ee} = \varepsilon_0 \alpha_{mm}$,[12,55,56]

and the magnitude of the quantity $\alpha_{ee} - \varepsilon_0\alpha_{mm}$ is plotted in log scale in Figure 2(b) as a function of radius and excitation wavelength, while κ is fixed at 0.1. The white dotted lines depict the conditions where the logarithm of $|\alpha_{ee} - \varepsilon_0\alpha_{mm}|$(normalized to maximum) has a value below -1.5 and the relation $\alpha_{ee} = \varepsilon_0\alpha_{mm}$ is approximately satisfied whereas the black dotted lines show the resonant position of electro-magnetic Mie coefficient c_1 as found in panel (a). The finite separation between the two curves assures that the Kerker condition is less likely to have any impact on helicity density measurements if the force difference measurement is properly maximized.

Full Wave Simulations

To further validate our analytical findings, we perform 3D full wave simulations to determine the force exerted on a chiral tip when it is placed above a dielectric substrate. We use the finite element method implemented in COMSOL Multiphysics. In the simulation, the tip is modeled as an isotropic chiral sphere[39,57,58] with the same material parameters as used above in Mie scattering formalism. Indeed, ε_r and μ_r of the sphere are same as that of silicon with $\mu_r = 1$ and the bulk chirality parameter is $\kappa = 0.1$. As shown in figure 3(a), the sphere is placed above a semi-infinite glass substrate ($n = 1.5$) and the distance between the glass surface and the sphere surface is 5 nm. The system is then sequentially illuminated by LCP and RCP plane waves of field strength 1.5×10^6 Vm^{-1}, corresponding to 3.0 $\mathrm{mW}/\mu\mathrm{m}^2$, in the bottom illumination scheme. The force exerted on the chiral sphere is determined by integrating the Maxwell's stress tensor over the outer surface of the tip (i.e., the sphere).[59]

Figures 3(b), (c), and (d) show the time averaged-force difference spectrum for spheres of radius of 50 nm, 60 nm, and 70 nm, respectively. The blue solid and dotted curves show the analytical result using equation (18) and equation (16), whereas the full-wave FEM result is indicated by the black solid line. For all three cases, the FEM simulation closely follows the analytical result obtained for the main dipolar mode, which is found at the longer

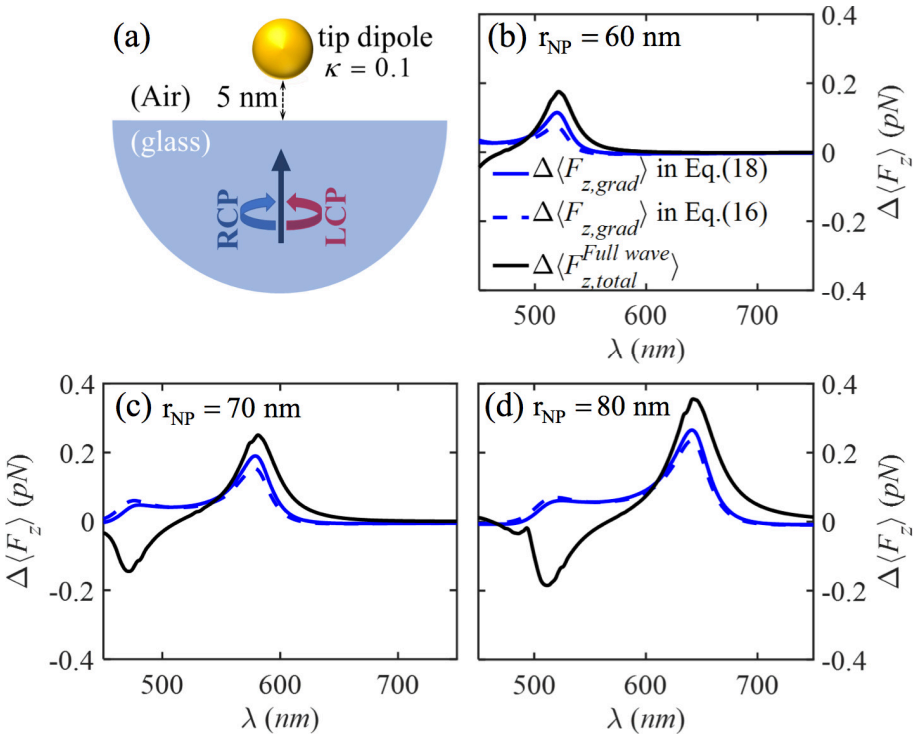

Figure 3: (a) Schematic of the chiral tip sphere above a glass substrate ($n = 1.5$) with radius r_{NP} and tip-surface and glass surface distance of 5 nm used in the FEM simulation. The material properties of the sphere, ε_r and μ_r are the same as silicon, with $\mu_r = 1$ and $\kappa = 0.1$. The system is illuminated by an incoming plane wave (first LCP then RCP) from below. Time-averaged differential gradient force from analytical calculation using equation 18 (blue solid) and equation 16 (blue dotted) and total force from full-wave simulations (black solid curve), for a chiral NP radius with radius (b) $r_{NP} = 50$ nm, (c) $r_{NP} = 60$ nm, and (d) $r_{NP} = 70$ nm.

wavelength and peaks with the Mie resonance of the c_1 coefficient. On resonance, the dipolar differential gradient force (blue curves) constitutes the dominant contribution to the total force difference (black curve). The dominance of the dipolar contribution grows more obvious as the radius is increased. The difference between the FEM simulation and the analytical results can be attributed to higher order multipole contributions, which are not considered in the dipolar approximation. The small difference between the solid and dotted blue curves is due to the contribution of z^{-5} distance dependent force term in equation (16). This term does not carry any information on the helicity density and its significance decreases for larger radii, as is evident in Figures 3(b)-(d). Near resonance, the differential force is of the order of 0.25 pN for the 80 nm radius tip ($\kappa = 0.1$). Although such forces are near the noise floor

of a typical PiFM microscope, sensitive experiments are likely able to resolve the targeted differental force under optimized conditions.[60]

The dip at lower wavelengths (black curve) for the 70 nm and 80 nm radius tips in Figure 3(c) and (d) is attributed to the differential interaction force, as defined in equation (17). This is because, equation (18) is positive-valued whereas (17) and the z^{-5} dependent term of equation (16) are negative-valued in the considered wavelength range. In the same lower wavelength region, the magnitude of $\Delta\langle F_{z,grad}\rangle$ is comparatively much smaller than the magnitude of $\Delta\langle F_{z,int}\rangle$ for the 70 nm and 80 nm radius tips.

Force Map of Helicity Density

Finally, we present the differential force map of the helicity density for a focused chiral beam, a scenario of direct relevance to microscopy applications. The situation is schematically shown in Figure 4(a) where an isotropic chiral sphere of radius $r_{NP} = 80$ nm is scanned over the focal region of the incident beams above glass substrate. We assume a circularly polarized Gaussian beam of 2 mW average power at a wavelength of $\lambda = 641$ nm as the incident light source, which is focused by a 1.4 NA oil ($n = 1.518$) objective lens. The focal plane electric and magnetic field components used in the simulation are obtained from reference [32], page 62. We first calculate the normalized helicity density distribution at the focal plane for a focused LCP beam, which is shown in 4(b). We next calculate the differential force $\Delta\langle F_{z,grad}\rangle$ using equation (18). In Figure 4(c), $\Delta\langle F_{z,grad}\rangle$ is shown for the case of a tip of radius $r_{NP} = 80$ nm. As equation (18) suggests, the force difference has the same spatial dependence as the non-zero helicity density of the focused LCP beam shown in Figure 4(b).

Last, we consider a chiral nanoprobe with properties as those of a helical carving of regular achiral tips.[37] Such chiral tips display dominant longitudinal chirality[61] and in the dipolar approximation this is reflected in the polarizabilty tensors as[46,61]

$$\begin{aligned}\underline{\boldsymbol{\alpha}}_{ee} &= \alpha_{ee}^{zz}\hat{\mathbf{z}}\hat{\mathbf{z}};\\ \underline{\boldsymbol{\alpha}}_{mm} &= \alpha_{mm}^{zz}\hat{\mathbf{z}}\hat{\mathbf{z}}\\ \underline{\boldsymbol{\alpha}}_{em} &= \alpha_{em}^{zz}\hat{\mathbf{z}}\hat{\mathbf{z}}\end{aligned} \tag{19}$$

Here we have ignored the non-diagonal components of the polarizability tensors for brevity. Such an approximation is reasonable as long as the helical axis is aligned along the main propagation axis. We note that even though the finite number of helical turns introduces non-zero elements of the polarizability tensor, such contributions are negligible compared to the dominant diagonal elements.[61] Under these conditions, the differential gradient force for the helical-shaped tip turns out be

$$\Delta\langle F_{z,grad}\rangle \sim \frac{6\omega c}{\pi|z|^4}\mathrm{Im}\Big\{\frac{\alpha_{em}^{zz*}}{\varepsilon_0}(\alpha_{ee}^{zz}-\alpha_{mm}^{zz}\varepsilon_0)\Big\}h_z^{inc} \tag{20}$$

The details of the derivation can be found in Supporting Information (SI Section 3). Interestingly, the differential gradient force for the helical-shaped tip is only sensitive to the longitudinal component of the helicity density. In contrast, the isotropic chiral tip measures both the transverse and longitudinal components in the differential force measurement, as expressed in equation (18).

To demonstrate these features, we consider a helical-shaped tip that is placed above a glass substrate, and subsequently scanned over the focal region as sketched in Figure 4(d). Figure 4(e) shows the calculated longitudinal component of the helicity density, revealing a donut shaped profile. Next, to calculate the differential force we use the same polarizability values of the isotropic chiral sphere in Figure 4(a) for α_{ee}^{zz}, α_{mm}^{zz} and α_{em}^{zz}. The map of $\Delta\langle F_{z,grad}\rangle$ for the helical-shaped tip is depicted in figure 4(f), showing the expected donut profile that replicates the longitudinal component of the helicity density of the incident LCP beam. In the Supporting Information, we also present the helicity density maps determined through the differential force of a focused azimuthally radially polarized beam (ARPB).[17,38,44]

We note that in principle, a proper design of the nanoprobe should also allow for mapping the transverse components of the helicity density. This would require a probe with polarizability elements $\alpha_{em}^{xx} \neq 0$ and/or $\alpha_{em}^{yy} \neq 0$ with $\alpha_{em}^{zz} = 0$, which can be accomplished if the chiral probe exhibits a helical current path in the transverse direction.

Conclusion

We have studied the information contained in the photo-induced force exerted on a chiral tip (modeled as a chiral nanosphere) when it is illuminated by chiral light. Our theoretical analysis reveals that the differential force is directly sensitive to the chiral properties of light. In particular, the dominant component to the differential gradient force is directly proportional to the helicity density of the incident chiral light, whereas the differential scattering force is sensitive solely to the spin angular momentum of the applied light. Using realistic values for the illumination intensity, tip dimension, and the chirality parameter of the tip, we find that the differential force can reach detectable values of several hundreds of fN, just above the noise floor of common scan probe microscopy systems. These findings are significant because a direct characterization of optical chirality at the nanoscale has hitherto been challenging. The observation that the differential gradient force can map out the local helicity density of the light is relevant for applications where knowledge of the chiral state of light at sub-diffraction-limited dimensions is important, including for sorting of chiral enantiomers with spatially confined light.

Funding Sources

This work was supported by the W. M. Keck Foundation, USA, and the National Science Foundation, grant CMMI-1905582.

Supporting Information Available

Detailed derivations are available in the Supporting Information.

References

(1) Tang, Y.; Cohen, A. E. Enhanced enantioselectivity in excitation of chiral molecules by superchiral light. Science **2011**, 332, 333–336.

(2) Zhao, Y.; Saleh, A. A.; Dionne, J. A. Enantioselective optical trapping of chiral nanoparticles with plasmonic tweezers. Acs Photonics **2016**, 3, 304–309.

(3) Gorkunov, M. V.; Darinskii, A. N.; Kondratov, A. V. Enhanced sensing of molecular optical activity with plasmonic nanohole arrays. JOSA B **2017**, 34, 315–320.

(4) Govorov, A. O.; Fan, Z.; Hernandez, P.; Slocik, J. M.; Naik, R. R. Theory of circular dichroism of nanomaterials comprising chiral molecules and nanocrystals: plasmon enhancement, dipole interactions, and dielectric effects. Nano letters **2010**, 10, 1374–1382.

(5) Govorov, A. O. Plasmon-induced circular dichroism of a chiral molecule in the vicinity of metal nanocrystals. Application to various geometries. The Journal of Physical Chemistry C **2011**, 115, 7914–7923.

(6) Amabilino, D. B. Chirality at the nanoscale: nanoparticles, surfaces, materials and more; John Wiley & Sons, 2009.

(7) Behr, J.-P. The lock-and-key principle: the state of the art–100 years on; John Wiley & Sons, 2008.

(8) Denmark, S. E.; Siegel, J. A. Topics in stereochemistry; John Wiley & Sons, 2006; Vol. 25.

(9) Tverdislov, V.; Malyshko, E.; Il'chenko, S.; Zhulyabina, O.; Yakovenko, L. A periodic system of chiral structures in molecular biology. Biophysics **2017**, 62, 331–341.

(10) Kasprzyk-Hordern, B. Pharmacologically active compounds in the environment and their chirality. Chemical Society Reviews **2010**, 39, 4466–4503.

(11) Ho, C.-S.; Garcia-Etxarri, A.; Zhao, Y.; Dionne, J. Enhancing enantioselective absorption using dielectric nanospheres. ACS Photonics **2017**, 4, 197–203.

(12) Hanifeh, M.; Capolino, F. Helicity maximization in a planar array of achiral high-density dielectric nanoparticles. Journal of Applied Physics **2020**, 127, 093104.

(13) Hanifeh, M.; Albooyeh, M.; Capolino, F. Helicity maximization below the diffraction limit. Physical Review B **2020**, 102, 165419.

(14) Bliokh, K. Y.; Bekshaev, A. Y.; Nori, F. Dual electromagnetism: helicity, spin, momentum and angular momentum. New Journal of Physics **2013**, 15, 033026.

(15) Cameron, R. P.; Barnett, S. M.; Yao, A. M. Optical helicity, optical spin and related quantities in electromagnetic theory. New Journal of Physics **2012**, 14, 053050.

(16) Trueba, J. L.; Ranada, A. F. The electromagnetic helicity. European Journal of Physics **1996**, 17, 141.

(17) Hanifeh, M.; Albooyeh, M.; Capolino, F. Optimally Chiral Light: Upper Bound of Helicity Density of Structured Light for Chirality Detection of Matter at Nanoscale. ACS Photonics **2020**, 7, 2682–2691.

(18) Bliokh, K. Y.; Nori, F. Characterizing optical chirality. Physical Review A **2011**, 83, 021803.

(19) Barnett, S. M. Rotation of electromagnetic fields and the nature of optical angular momentum. Journal of modern optics **2010**, 57, 1339–1343.

(20) Tang, Y.; Cohen, A. E. Optical chirality and its interaction with matter. Physical review letters **2010**, 104, 163901.

(21) Lee, K.; Kihm, H.; Kihm, J.; Choi, W.; Kim, H.; Ropers, C.; Park, D.; Yoon, Y.; Choi, S.; Woo, D., et al. Vector field microscopic imaging of light. Nature Photonics **2007**, 1, 53–56.

(22) Grosjean, T.; Ibrahim, I.; Suarez, M.; Burr, G.; Mivelle, M.; Charraut, D. Full vectorial imaging of electromagnetic light at subwavelength scale. Optics Express **2010**, 18, 5809–5824.

(23) Le Feber, B.; Rotenberg, N.; Beggs, D. M.; Kuipers, L. Simultaneous measurement of nanoscale electric and magnetic optical fields. Nature Photonics **2014**, 8, 43–46.

(24) Bauer, T.; Orlov, S.; Peschel, U.; Banzer, P.; Leuchs, G. Nanointerferometric amplitude and phase reconstruction of tightly focused vector beams. Nature Photonics **2014**, 8, 23–27.

(25) Zeng, J.; Albooyeh, M.; Rajaei, M.; Sifat, A. A.; Potma, E. O.; Wickramasinghe, H. K.; Capolino, F. Photoinduced Magnetic Force Microscopy: Enabling Direct and Exclusive Detection of Optical Magnetism. arXiv, July 10, 2021; `https://arxiv.org/abs/2107.04739`, accessed 2022-02-10.

(26) Emile, O.; Emile, J. Energy, Linear Momentum, and Angular Momentum of Light: What Do We Measure? Annalen der Physik **2018**, 530, 1800111.

(27) Neugebauer, M.; Eismann, J. S.; Bauer, T.; Banzer, P. Magnetic and electric transverse spin density of spatially confined light. Physical Review X **2018**, 8, 021042.

(28) Zeng, J.; Huang, F.; Guclu, C.; Veysi, M.; Albooyeh, M.; Wickramasinghe, H. K.; Capolino, F. Sharply focused azimuthally polarized beams with magnetic domi-

nance: near-field characterization at nanoscale by photoinduced force microscopy. ACS Photonics **2018**, 5, 390–397.

(29) Huang, F.; Ananth Tamma, V.; Mardy, Z.; Burdett, J.; Kumar Wickramasinghe, H. Imaging nanoscale electromagnetic near-field distributions using optical forces. Scientific reports **2015**, 5, 1–12.

(30) Hou, S.; Liu, Y.; Zhang, W.; Zhang, X. Separating and trapping of chiral nanoparticles with dielectric photonic crystal slabs. Optics Express **2021**, 29, 15177–15189.

(31) Kamenetskii, E. Chirality, Magnetism and Magnetoelectricity: Separate Phenomena and Joint Effects in Metamaterial Structures; Springer Nature, 2021; Vol. 138.

(32) Hayat, A.; Mueller, J. B.; Capasso, F. Lateral chirality-sorting optical forces. Proceedings of the National Academy of Sciences **2015**, 112, 13190–13194.

(33) Tkachenko, G.; Brasselet, E. Optofluidic sorting of material chirality by chiral light. Nature communications **2014**, 5, 1–7.

(34) Li, M.; Yan, S.; Zhang, Y.; Liang, Y.; Zhang, P.; Yao, B. Optical sorting of small chiral particles by tightly focused vector beams. Physical Review A **2019**, 99, 033825.

(35) Kamandi, M.; Albooyeh, M.; Guclu, C.; Veysi, M.; Zeng, J.; Wickramasinghe, K.; Capolino, F. Enantiospecific detection of chiral nanosamples using photoinduced force. Physical Review Applied **2017**, 8, 064010.

(36) Rajaei, M.; Zeng, J.; Albooyeh, M.; Kamandi, M.; Hanifeh, M.; Capolino, F.; Wickramasinghe, H. K. Giant circular dichroism at visible frequencies enabled by plasmonic ramp-shaped nanostructures. ACS Photonics **2019**, 6, 924–931.

(37) Zhao, Y.; Saleh, A. A.; Van De Haar, M. A.; Baum, B.; Briggs, J. A.; Lay, A.; Reyes-Becerra, O. A.; Dionne, J. A. Nanoscopic control and quantification of enantioselective optical forces. Nature nanotechnology **2017**, 12, 1055–1059.

(38) Novotny, L.; Hecht, B. Principles of nano-optics; Cambridge university press, 2012.

(39) Yang, H. U.; Raschke, M. B. Resonant optical gradient force interaction for nano-imaging and-spectroscopy. New Journal of Physics **2016**, 18, 053042.

(40) Nieto-Vesperinas, M.; Sáenz, J.; Gómez-Medina, R.; Chantada, L. Optical forces on small magnetodielectric particles. Optics express **2010**, 18, 11428–11443.

(41) Yaghjian, A. D. Electromagnetic forces on point dipoles. IEEE Antennas and Propagation Society International Symposium. 1999 Digest. Held in conjunction with: USNC/URSI National Radio Science Meeting (Cat. No. 99CH37010). 1999; pp 2868–2871.

(42) Tai, C.; Antennas, I.; Society, P.; Theory, I. M.; Society, T. Dyadic Green Functions in Electromagnetic Theory; IEEE Press Publication Series; IEEE Press, 1994.

(43) Wang, S. B.; Chan, C. T. Lateral optical force on chiral particles near a surface. Nature Communications **2014**, 5, 1–8.

(44) Kamandi, M.; Albooyeh, M.; Veysi, M.; Rajaei, M.; Zeng, J.; Wickramasinghe, H. K.; Capolino, F. Unscrambling structured chirality with structured light at the nanoscale using photoinduced force. ACS Photonics **2018**, 5, 4360–4370.

(45) Zeng, J.; Darvishzadeh-Varcheie, M.; Albooyeh, M.; Rajaei, M.; Kamandi, M.; Veysi, M.; Potma, E. O.; Capolino, F.; Wickramasinghe, H. Exclusive magnetic excitation enabled by structured light illumination in a nanoscale Mie resonator. ACS nano **2018**, 12, 12159–12168.

(46) Serdyukov, A.; Semchenko, I.; Tertyakov, S.; Sihvola, A. Electromagnetics of bi-anisotropic materials - Theory and Application; Electrocomponent Science Monographs; Gordon and Breach Science Publishers, 2001; Vol. 11.

(47) Jackson, J. D. Classical electrodynamics; John Wiley & Sons, 1975.

(48) Rajapaksa, I.; Uenal, K.; Wickramasinghe, H. K. Image force microscopy of molecular resonance: A microscope principle. Applied physics letters **2010**, 97, 073121.

(49) Campione, S.; Sinclair, M. B.; Capolino, F. Effective medium representation and complex modes in 3D periodic metamaterials made of cubic resonators with large permittivity at mid-infrared frequencies. Photonics and Nanostructures-Fundamentals and Applications **2013**, 11, 423–435.

(50) Jahng, J.; Brocious, J.; Fishman, D. A.; Huang, F.; Li, X.; Tamma, V. A.; Wickramasinghe, H. K.; Potma, E. O. Gradient and scattering forces in photoinduced force microscopy. Physical Review B **2014**, 90, 155417.

(51) Bohren, C. F. Univ. of Arizona, Dept. of Physics. Light Scattering by Irregularly Shaped Particles **2012**, 103.

(52) Aspnes, D. E.; Studna, A. Dielectric functions and optical parameters of si, ge, gap, gaas, gasb, inp, inas, and insb from 1.5 to 6.0 ev. Physical review B **1983**, 27, 985.

(53) Ali, R.; Pinheiro, F. A.; Dutra, R. S.; Rosa, F. S.; Neto, P. A. M. Enantioselective manipulation of single chiral nanoparticles using optical tweezers. Nanoscale **2020**, 12, 5031–5037.

(54) Ali, R.; Pinheiro, F.; Dutra, R.; Rosa, F.; Neto, P. M. Probing the optical chiral response of single nanoparticles with optical tweezers. JOSA B **2020**, 37, 2796–2803.

(55) Kerker, M.; Wang, D.-S.; Giles, C. Electromagnetic scattering by magnetic spheres. JOSA **1983**, 73, 765–767.

(56) Lee, J. Y.; Miroshnichenko, A. E.; Lee, R.-K. Reexamination of Kerker's conditions by means of the phase diagram. Physical Review A **2017**, 96, 043846.

(57) Nieto-Vesperinas, M.; Chaumet, P.; Rahmani, A. Near-field photonic forces.

Philosophical Transactions of the Royal Society of London. Series A: Mathematical, Physical and Engineering Sciences **2004**, 362, 719–737.

(58) Chu, P.; Mills, D. L. Laser-Induced Forces in Metallic Nanosystems: The Role of Plasmon Resonances. Phys. Rev. Lett. **2007**, 99, 127401.

(59) Yang, H. U.; Raschke, M. B. Resonant optical gradient force interaction for nanoimaging and -spectroscopy. New Journal of Physics **2016**, 18, 053042.

(60) Yamanishi, J.; Yamane, H.; Naitoh, Y.; Li, Y. J.; Yokoshi, N.; Kameyama, T.; Koyama, S.; Torimoto, T.; Ishihara, H.; Sugawara, Y. Optical force mapping at the single-nanometre scale. Nature Communications **2021**, 12, 1–7.

(61) Caloz, C.; Sihvola, A. Electromagnetic chirality, Part 1: the microscopic perspective [electromagnetic perspectives]. IEEE Antennas and Propagation Magazine **2020**, 62, 58–71.

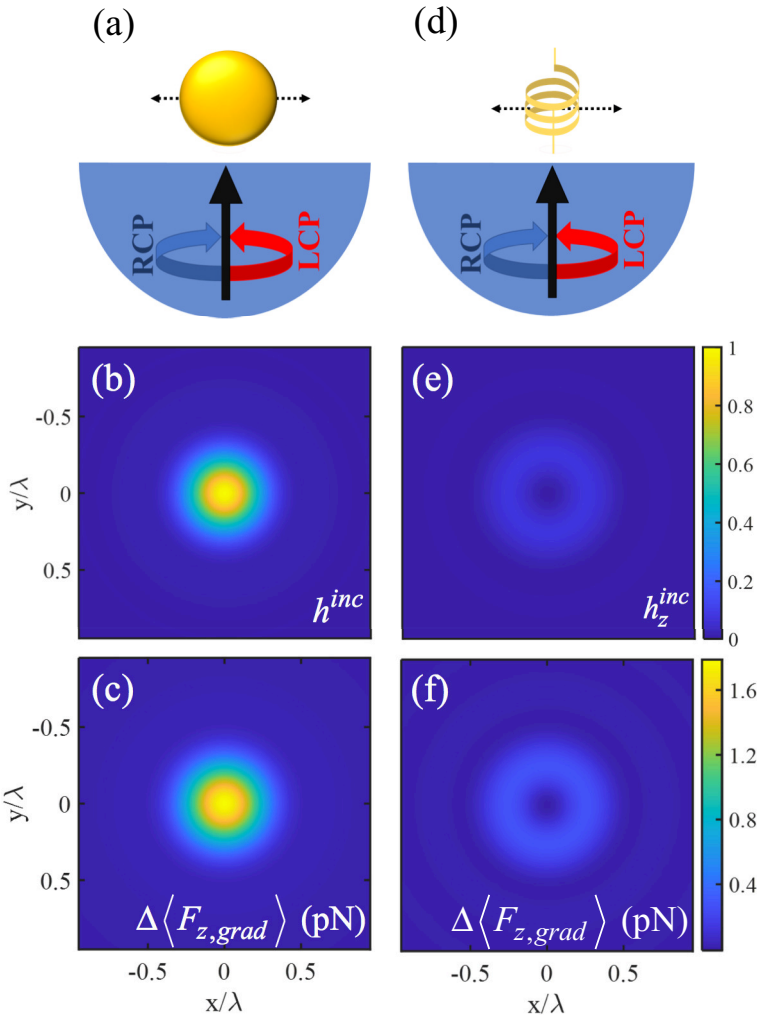

Figure 4: (a) Sketch of an isotropic chiral scatterer being horizontally scanned over a glass substrate through the focus of a circularly polarized (LCP/RCP) beam. (b) The focal plane distribution of total normalized helicity density ($h^{inc} = \frac{1}{2\omega c}\mathrm{Im}\{\mathbf{E^{inc}} \cdot \mathbf{H^{inc*}}\}$) of the incident circularly polarized (LCP) light focused by a 1.4 NA oil objective. (c) The differential force map, $\Delta\langle F_{z,grad}\rangle$ at the focal plane for a chiral isotropic tip of radius $r_{NP} = 80$ nm. (d) Sketch of a helical-shaped tip in the same configuration as in (a). (e) Spatial dependence of the longitudinal component of the normalized helicity density ($h_z^{inc} = \frac{1}{2\omega c}\mathrm{Im}\{E_z^{\mathrm{inc}} H_z^{\mathrm{inc*}}\}$) in (b). (f) Differential force map for the helical-shaped tip. The polarizability strength of the isotropic and helical-shaped tip has been set to the same value.